STRUCTURAL BIOLOGY
ISSN 2059-7983

X-ray structure of the metastable SEPT14–SEPT7 coiled coil reveals a hendecad region crucial for heterodimerization

Italo A. Cavini,[a] Ashley J. Winter,[b] Humberto D'Muniz Pereira,[a] Derek N. Woolfson,[b,c,d] Matthew P. Crump[b,d] and Richard C. Garratt[a]*

[a]São Carlos Institute of Physics, University of São Paulo, Avenida João Dagnone 1100, São Carlos, SP 13563-120, Brazil, [b]School of Chemistry, University of Bristol, Cantock's Close, Bristol BS8 1TS, United Kingdom, [c]School of Biochemistry, University of Bristol, Medical Sciences Building, University Walk, Bristol BS8 1TD, United Kingdom, and [d]BrisSynBio, University of Bristol, School of Chemistry, Bristol BS8 1TS, United Kingdom. *Correspondence e-mail: richard@ifsc.usp.br

Received 11 May 2023
Accepted 27 July 2023

Edited by B. Kobe, University of Queensland, Australia

Keywords: coiled coils; hendecad repeats; heterodimerization; metastability; septins.

PDB reference: metastable SEPT14–SEPT7 heterodimeric coiled coil, 8sjj

SASBDB references: MBP-SEPT6c + SUMO-SEPT7c, SASDR39; MBP-SEPT8c + SUMO-SEPT7c, SASDR49; MBP-SEPT10c + SUMO-SEPT7c, SASDR59; MBP-SEPT11c + SUMO-SEPT7c, SASDR69; MBP-SEPT14c + SUMO-SEPT7c, SASDR79

Supporting information: this article has supporting information at journals.iucr.org/d

Septins are membrane-associated, GTP-binding proteins that are present in most eukaryotes. They polymerize to play important roles as scaffolds and/or diffusion barriers as part of the cytoskeleton. α-Helical coiled-coil domains are believed to contribute to septin assembly, and those observed in both human SEPT6 and SEPT8 form antiparallel homodimers. These are not compatible with their parallel heterodimeric organization expected from the current model for protofilament assembly, but they could explain the interfilament cross-bridges observed by microscopy. Here, the first structure of a heterodimeric septin coiled coil is presented, that between SEPT14 and SEPT7; the former is a SEPT6/SEPT8 homolog. This new structure is parallel, with two long helices that are axially shifted by a full helical turn with reference to their sequence alignment. The structure also has unusual knobs-into-holes packing of side chains. Both standard seven-residue (heptad) and the less common 11-residue (hendecad) repeats are present, creating two distinct regions with opposite supercoiling, which gives rise to an overall straight coiled coil. Part of the hendecad region is required for heterodimerization and therefore may be crucial for selective septin recognition. These unconventional sequences and structural features produce a metastable heterocomplex that nonetheless has enough specificity to promote correct protofilament assembly. For instance, the lack of supercoiling may facilitate unzipping and transitioning to the antiparallel homodimeric state.

1. Introduction

1.1. Septins

Septins are conserved proteins that are found in most eukaryotes, except vascular plants. As part of the cytoskeleton, they participate in a wide diversity of remodelling events affecting cell morphology, including cytokinesis, the formation of phagosomes and diffusion barriers and the entrapment of bacteria, to mention just a few (Hartwell, 1971; Hu *et al.*, 2010; Mostowy & Cossart, 2012; Robertin & Mostowy, 2020). The canonical septin fold has three domains: an N-terminal domain (NTD), a GTP-binding domain (G) and a C-terminal domain (CTD) that frequently contains coiled-coil (CC) repeats (Versele *et al.*, 2004). In humans, 13 septins have been identified (SEPT1–SEPT12 and SEPT14) and have been classified into four groups according to their sequence similarity: the SEPT2, SEPT6, SEPT7 and SEPT3 groups (Martinez & Ware, 2004; Pan *et al.*, 2007). The SEPT7 group is the smallest, with SEPT7 as the sole member, and the SEPT6

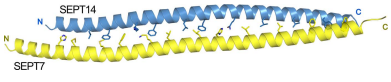

group is the largest, being composed of SEPT6, SEPT8, SEPT10, SEPT11 and SEPT14.

SEPT14, the last to be identified, is highly enriched in the testis (Peterson *et al.*, 2007; Uhlén *et al.*, 2015). Low expression levels of SEPT14 in sperm have been linked to male infertility due to a likely role in human spermatogenesis (Shafipour *et al.*, 2014; Vahabi Barzi *et al.*, 2020). Interestingly, two point mutations in SEPT14, A123T and I333T (with the latter being localized in the CTD), can cause defects in the sperm head and nucleus (Wang *et al.*, 2019; Lin *et al.*, 2020).

All septin functions are related to their ability to heteropolymerize into organized filamentous structures including, but not limited to, paired filaments, gauzes and rings (Bertin *et al.*, 2008; Ong *et al.*, 2014). From two to four different septins assemble into a palindromic linear heterooligomer (or protofilament) containing two copies of each subunit. These represent the building blocks for polymerization. For the human septins, both hexamers (of the type SEPT2–SEPT6–SEPT7–SEPT7–SEPT6–SEPT2) and octamers (SEPT2–SEPT6–SEPT7–SEPT3–SEPT3–SEPT7–SEPT6–SEPT2) can form, and the internal order of these subunits has recently been revised (Sirajuddin *et al.*, 2007; Kim *et al.*, 2011; Sellin *et al.*, 2011; Mendonça *et al.*, 2019; Soroor *et al.*, 2021). These protofilaments subsequently polymerize into filaments via interactions involving the terminal copies of SEPT2. It is believed that septins from the same group occupy the same relative position within filaments, giving rise to a wide range of viable combinations, a principle known as Kinoshita's rule (Kinoshita, 2003; Valadares *et al.*, 2017; Mendonça *et al.*, 2019).

Septin subunits within a filament interact via two different kinds of interfaces; one, the NC interface, potentially involves CC formation (Fig. 1*a*). Two different CC-containing NC interfaces are expected: the homodimeric NC interface, formed when oligomers polymerize end to end (for example SEPT2–SEPT2), and the heterodimeric NC interface, which is internal to the protofilament (for example SEPT6–SEPT7). Kinoshita's rule implies that SEPT6 at this latter type of interface could be replaced by SEPT8, SEPT10, SEPT11 or SEPT14, giving rise to five possible types of heterodimer with SEPT7. The structure of the SEPT2G–SEPT6–SEPT7 complex solved by cryo-electron microscopy (Mendonça *et al.*, 2021; Fig. 1*a*) used intact SEPT6 and SEPT7, but did not reveal the organization of these CTDs as they were disordered with respect to the protofilament axis (Cavini *et al.*, 2021).

As a result, septin CTDs have been studied in isolation from other septin domains. It has been shown that the CTDs of SEPT6, SEPT8, SEPT10 and SEPT11 can form heterocomplexes with the SEPT7 CTD with dissociation constants in the low-nanomolar range (de Almeida Marques *et al.*, 2012; Sala *et al.*, 2016). These complexes are essentially heterodimers and fluorescence resonance energy transfer (FRET) experiments indicate that the CC formed between SEPT6 and SEPT7 is parallel (Low & Macara, 2006). In the absence of their partner, the CTDs form low-affinity homodimers (de Almeida Marques *et al.*, 2012; Sala *et al.*, 2016). Recently, we have reported the homodimeric CC structures of SEPT6 (PDB entry 6wbp) and SEPT8 (PDB entry 6wsm) (Leonardo *et al.*, 2021). Both are similar antiparallel CCs with charged residues at *a* positions intercalated favourably on the same side of the CC. This antiparallel arrangement led us to speculate on the possibility that these homodimeric structures may form the cross-bridges seen between septin filaments (Bertin *et al.*, 2008, 2010; Jiao *et al.*, 2020; Szuba *et al.*, 2021; Leonardo *et al.*, 2021; Fig. 1*b*). Similarly, SEPT2 CTDs may form antiparallel homodimeric coiled coils which could connect filaments with a tighter spacing, due to their shorter length (Leonardo *et al.*, 2021).

1.2. Coiled-coil motifs

α-Helical coiled coils (CCs) are one of the best understood tertiary/quaternary structures in proteins (Lupas & Gruber, 2005; Woolfson, 2017, 2023; Lupas & Bassler, 2017). This understanding stems from their apparent sequence and structural simplicity, although new variations and architectures are being uncovered (Lupas & Bassler, 2017; Beesley & Woolfson, 2019). CCs are bundles of two or more α-helices with parallel, antiparallel or mixed arrangements around a central superhelical axis. At the sequence level, these are mostly encoded by seven-residue or heptad repeats (*a*-*b*-*c*-*d*-*e*-*f*-*g*), which span approximately two helical turns and usually have hydrophobic residues at the *a* and *d* positions. This is referred to as 7/2 periodicity (Lupas, 1996). Because the number of residues per turn of right-handed α-helices (3.6) is greater than the periodicity of hydrophobic residues (3.5), the resulting amphipathic α-helices wrap around each other with a left-handed twist or supercoil. This also leads to the structural hallmark of CCs, namely knobs-into-holes (KIH) packing between helices, where the side chains at the *a* and *d* sites (the knobs) from one helix pack into diamond-shaped holes formed by four side chains from another helix (Crick, 1952, 1953). In parallel, in-register CC dimers this results in *a*–*a* and *d*–*d* core layers with so-called parallel and perpendicular packing geometries, respectively, and another geometry, acute packing, occurs in trimers (Harbury *et al.*, 1993; Supplementary Fig. S1).

Other CC sequence repeats and periodicities exist (Pauling & Corey, 1953; Brown *et al.*, 1996; Hicks *et al.*, 1997; Lupas & Gruber, 2005), for example hendecads (11/3) and pentadecads (15/4). These directly impact the supercoil. For instance, in hendecad repeats (*a*-*b*-*c*-*d*-*e*-*f*-*g*-*h*-*i*-*j*-*k*) the spacing between core-packing/hydrophobic sites at *a*, *d* and *h* is 11/3 or 3.67 residues. As this is slightly greater than the fixed rise per residue of the α-helix, the resulting CCs have a right-handed twist, although this supercoiling is less pronounced than in heptad-based structures. This arrangement was originally identified in the sequence of tetrabrachion (Peters *et al.*, 1996) and later its structure (PDB entry 1fe6; Stetefeld *et al.*, 2000), and has been developed generally by others (Brown *et al.*, 1996; Hicks *et al.*, 1997; Lupas & Gruber, 2005). Inevitably, this departure from the canonical and idealized sequence motifs also affects core packing, resulting in so-called *x* and/or *da* geometries (Lupas & Gruber, 2005).

A valuable measure to characterize and parameterize CCs is the Crick angle or positional orientation angle φ (Supplementary Fig. S1). Axial rotations ($\Delta\varphi$) of the helices may lead to less common Crick angles of core residues; these include the above arrangements *x* (a residue halfway between the *a* and *d* canonical positions) and *da* (where two consecutive residues are part of the core) (Lupas & Gruber, 2005). In symmetric homo-oligomers, knob-to-knob (KTK) contacts can preclude the pairing of residues other than alanines and glycines (Lupas & Gruber, 2005). However, relaxation of the structural constraints, such as antiparallel structures and register shifts, can allow larger side chains in positions with the *x* geometry (Lupas & Gruber, 2005). Notably, even identical helices can break symmetry and pack offset along the

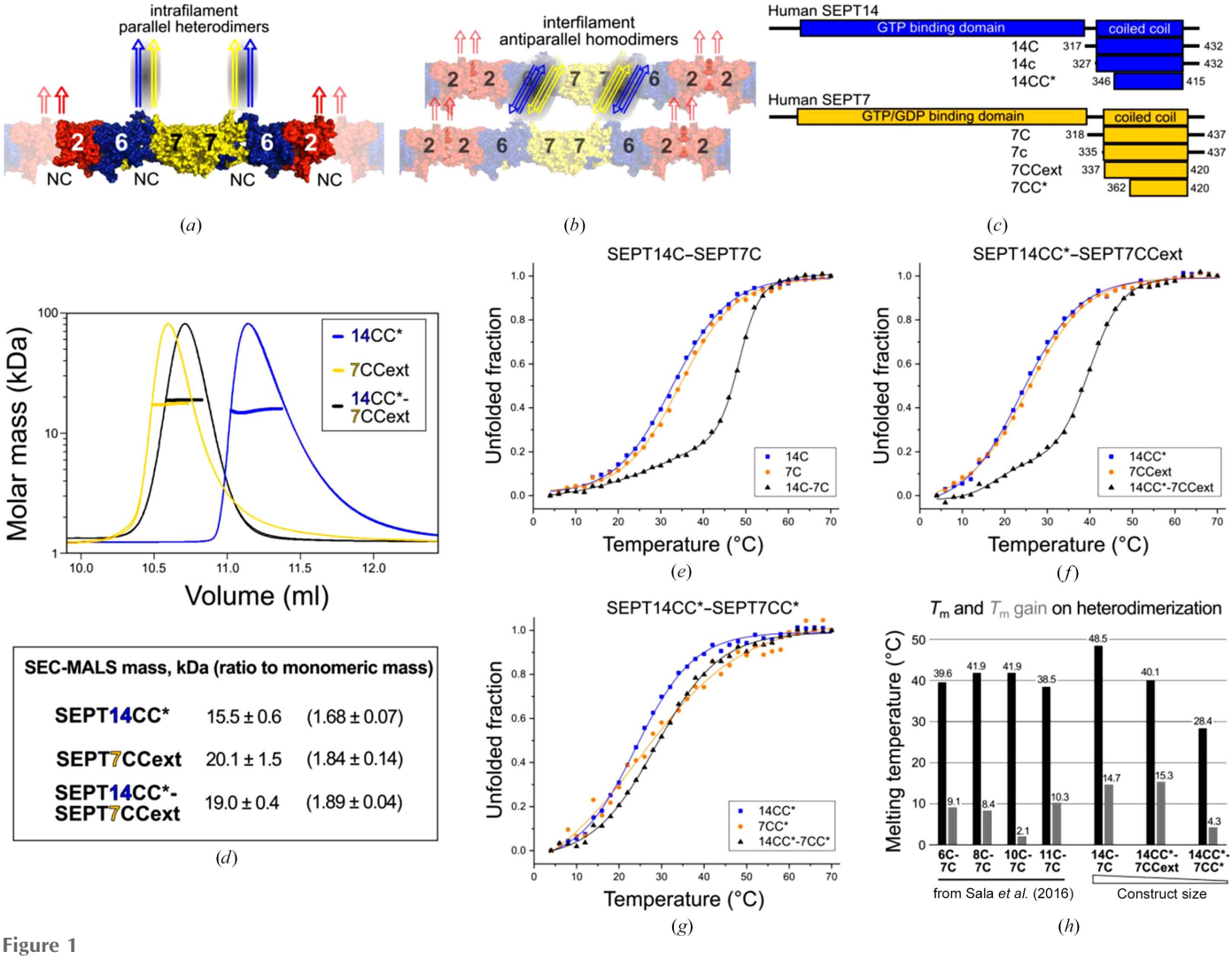

Figure 1
Characterization of the oligomeric state and heterodimerization of the CC constructs. (*a*) Septin protofilament organization according to the cryo-EM structure of the SEPT2G–SEPT6–SEPT7 complex (PDB entry 7m6j). Protofilaments polymerize end to end (adjacent protofilaments are shown semi-transparent) and their NC interfaces are depicted. The CTDs (arrows) are not modelled/present within the structure but are expected to project as indicated from the stubs at the C-termini of the corresponding G domains. (*b*) 'Railroad-track' model in which the CTDs of SEPT6 (and maybe SEPT7) form antiparallel homodimeric coiled coils connecting different filaments. (*c*) Human septins SEPT14 and SEPT7 have a central Ras-like G domain and a CC sequence within the CTD (boxes). The constructs used and their truncation positions are shown. (*d*) Septin CC constructs are predominantly dimeric by SEC-MALS. Thin lines represent the normalized UV absorption and differential refractive index, whereas thick lines represent the molar mass. The peptide concentration at injection was 0.8 m*M* (0.4 m*M* each in the case of the equimolar mixture). SEPT14CC* elutes as a single peak corresponding to a mixture of dimers and monomers (roughly 2:1, considering the calculated mass) as also demonstrated by the tail associated with the elution profile. To a lesser extent, SEPT7CCext also presents peak tailing and dimeric mass underestimation. The SEPT14CC*–SEPT7CCext mixture behaves essentially as dimers. (*e*) CD thermal denaturations of the complete CTDs, SEPT14C, SEPT7C (10 µ*M*) and their equimolar mixture (5 µ*M* each, 10 µ*M* total). (*f*) SEPT14CC*–SEPT7CCext (10 µ*M* total). The presence of residual homodimers and/or monomers cannot be ruled out, potentially explaining the minor transition at around 20°C. (*g*) SEPT14CC*–SEPT7CC* (10 µ*M* total). There is a considerable gain in the melting temperature in the longer constructs, but not in the case of the SEPT14CC*–SEPT7CC* mixture, as SEPT7CC* is overtruncated (12 residues shorter than SEPT14CC*). (*h*) Comparison of the melting temperatures (T_m, black bars) and T_m gain (grey bars) found by CD for the different SEPT6-group CTDs when mixed with the SEPT7 CTD (Sala *et al.*, 2016) and the different constructs involving SEPT14 and SEPT7 (reported here). The complex formed by the SEPT14 and SEPT7 CTDs has the highest thermal stability among them. 'T_m gain' refers to the difference between the experimental T_m for the mixture and the predicted T_m for a mixture of the two individual samples (see Section 2).

superhelical axis, with shifts ranging from one register position (Harrison *et al.*, 1997) to a full α-helical turn (Liu *et al.*, 2006; Noell *et al.*, 2019).

Here, we present the X-ray crystal structure of a parallel heterodimeric septin CC formed between SEPT14 and SEPT7. This CC is unusual in several respects, including the presence of two regions with different periodicities (hendecads and heptads), a lack of supercoiling, offset helices and several aromatic residues in the core. The *x* and *da* packings of hendecads continue into the heptad region, generating a rare side-chain packing for parallel CCs in which the *d* positions of one helix interact with *a* and *g* positions in the other (*d-ag* cores). These results have implications for both subunit recognition and CC dynamics relevant to the assembly of higher-order septin arrangements.

2. Methods

2.1. Sample production

We used the full CTDs (dubbed 'C') of SEPT14 (UniProt Q6ZU15) and SEPT7 (UniProt Q16181) and different constructs containing only the full coiled-coil (CC) region ('CCext') or truncations of this ('CC*'). All protein sequences used are presented in Supplementary Table S1 and depicted in Fig. 1(*c*). SEPT7C (residues 318–437), SEPT7CCext (residues 337–420) and SEPT7CC* (residues 362–420, dubbed SEPT7CC in previous publications) have been used in previous work (de Almeida Marques *et al.*, 2012; Sala *et al.*, 2016; Leonardo *et al.*, 2021; Castro *et al.*, 2023). DNA sequences encoding SEPT14C (residues 317–432) and SEPT14CC* (residues 346–415) were amplified using *Taq* high-fidelity DNA polymerase (Cellco) from a commercially sourced plasmid (SEPT14, GenScript) or a reverse-transcribed sequence (SEPT7, NCBI entry BC093640.1) as templates. Purified inserts were digested using NdeI, XhoI and DpnI restriction enzymes (Fast Digest, Thermo) and ligated (T4 DNA ligase, Promega) into pre-digested pET-28a plasmids. Positive colonies had their insert DNA sequence confirmed using a 3130 Genetic Analyser DNA sequencer (Applied Biosystems).

MBP- and SUMO-fused constructs were designed and used in the SEC–SAXS experiments (see below). CTDs excluding the hinge (the region connecting the G-domain to the CC region), dubbed 'c' here, fused to an MBP or SUMO tag using tripeptide linkers (Ser-Gly-Ser and Gly-Ser-Ser in the MBP-fused and SUMO-fused constructs, respectively) were generated with the In-Fusion HD Cloning Kit (Takara). The following truncations were used: SEPT6c (residues 317–427, UniProt Q14141-2), SEPT7c (residues 335–437, UniProt Q16181), SEPT8c (residues 319–429, UniProt Q92599-2), SEPT10c (residues 341–454, UniProt Q9P0V9), SEPT11c (residues 316–429, UniProt Q9NVA2) and SEPT14c (residues 327–432, UniProt Q6ZU15). The pOPINM vector (coding for a His tag and MBP at the N-terminus) was amplified by KAPA HiFi HotStart DNA Polymerase (Kapa Biosystems) with the fidelity buffer plus 5% DMSO. The pET-SUMO vector (coding for SUMO at the N-terminus and a His tag at the C-terminus) and the inserts were amplified by Phusion Hot Start II High-Fidelity PCR Master Mix (Thermo Fisher) using the recommended PCR timings and temperatures. NEB5α cells were transformed with the reaction and the DNA sequences of positive clones were confirmed by DNA sequencing (Genewiz).

All peptides were produced according to our previous report (Leonardo *et al.*, 2021) unless stated otherwise. In brief, *Escherichia coli* Rosetta(DE3) cells were grown at 37°C in LB medium and protein expression was carried out overnight at 18°C by induction with 0.2 m*M* isopropyl β-D-1-thiogalactopyranoside when the $OD_{600\ nm}$ reached 0.6–0.8. The cells were harvested, solubilized in 50 m*M* Tris pH 8.0, 1 *M* NaCl, 10 m*M* imidazole and lysed by sonication. The clarified cellular extract was applied onto IMAC resin (Ni–NTA Superflow, Qiagen or TALON, Clontech), which was thoroughly washed with 10 column volumes (CV) of lysis buffer and subsequently with buffer containing 35 m*M* imidazole (5 CV). The protein was eluted in buffer containing 200 m*M* imidazole (usually in 5 CV). Thrombin was added for His-tag removal (3 U per milligram of protein) and the sample was dialysed overnight against 25 m*M* Tris pH 8.0, 500 m*M* NaCl. After cleavage, Benzamidine Sepharose 4 Fast Flow (GE Healthcare) and IMAC resins were used to remove thrombin and hexahistidine-containing peptides, respectively. Samples were concentrated (Amicon, Merck) and applied onto Superdex 75 size-exclusion columns (10/300 and HiLoad 16/600 for SEPT14 and SEPT7 constructs, respectively). The final sample buffer was 20 m*M* Tris pH 8.0, 300 m*M* NaCl. Sample purity was analysed by tricine–SDS–PAGE.

The procedure was similar for the MBP-fused and SUMO-fused constructs, except that expression was performed in T7 Express cells (NEB), purification was carried out with a HisTrap HP column (Cytiva) using 5% glycerol added to the purification buffer and a Superdex 200 Increase 10/300 GL column (Cytiva) was employed to purify the intact expressed proteins (*i.e.* without protease treatment). Sample purity was checked by SDS–PAGE.

In both protocols, to produce heteromeric samples, the two peptides/proteins were mixed in equimolar proportions after purification.

2.2. Oligomeric state analysed by SEC-MALS

For multi-angle light scattering coupled with size-exclusion chromatography (SEC-MALS), the light scattering and the differential refractive index were analysed with a miniDAWN TREOS and OptiLab T-rEX system (Wyatt). A Superdex 75 GL 10/300 column (GE Healthcare) was employed, using 20 m*M* Tris pH 7.8, 300 m*M* NaCl as the buffer. The peptide concentration used was 0.8 m*M* (0.4 m*M* of each peptide in the case of sample mixtures). Data were processed using the *ASTRA*7 software (Wyatt) for the determination of molecular masses and thereby oligomeric states.

2.3. Heteromerization analysis by circular dichroism spectroscopy

Midpoint melting temperatures (T_m), determined using circular dichroism (CD) spectroscopy, were used to evaluate the formation of heterodimers. CD measurements were recorded with a J-815 spectropolarimeter (Jasco) using 20 m*M* sodium phosphate, 50 m*M* NaCl pH 7.5 as the buffer. In the case of cysteine-containing peptide sequences, 1 m*M* DTT was added. Buffer exchange was achieved by sample dilution at a ratio of 100-fold or greater. Thermal denaturation experiments were performed by monitoring the CD signal at 222 nm using a bandwidth of 1 nm. The temperature was ramped from 4 to 70°C using a Peltier control module with data pitch of 2°C and a temperature slope of 1°C min^{-1}. The signal from the cuvette and buffer was subtracted from the peptide signal and the corrected data points were fitted using either a Boltzmann or a double Boltzmann function to extract the melting temperature T_m. The CD spectra of the individual species were averaged and the resultant denaturation curve was fitted to obtain the expected T_m for the case where no interaction was present; this T_m was used as a benchmark for comparison with the experimental T_m values of mixtures.

2.4. Coiled-coil orientation analysis by SEC–SAXS

Small-angle X-ray scattering coupled with size-exclusion chromatography (SEC–SAXS) experiments were performed on beamline B21 at the Diamond Light Source (DLS), Didcot, United Kingdom (Cowieson *et al.*, 2020) with an Agilent 1200 HPLC and a Superdex 200 Increase 3.2/300 column (GE Healthcare). Samples at a total protein concentration of 5 mg ml^{-1} (45 µl) were injected and run in 50 m*M* Tris, 150 m*M* NaCl pH 7.5 buffer. 1 m*M* dithiothreitol (DTT) was added to the buffer in cysteine-containing samples (SEPT14). X-ray scattering was recorded every 3 s at 15°C with an EIGER X 4M detector (Dectris) at a fixed camera length of 3.7209 m at 13.1 keV (corresponding to λ = 0.9464 Å). Angular q-range data were collected between 0.0045 and 0.34 Å^{-1} using a photon flux of 4×10^{12} s^{-1}. Data reduction, buffer subtraction and modelling of the radius of gyration (R_g), the maximum particle dimension (D_{max}) and the pair distance distribution function [$P(r)$] were determined using *Scatter IV* (Tully *et al.*, 2021) and *BioXTAS RAW* (Hopkins *et al.*, 2017). Mass estimations were performed using Bayesian inference (Hajizadeh *et al.*, 2018), *SAXSMoW* (Fischer *et al.*, 2010) and volume of correlation (Rambo & Tainer, 2013) methods. *FoXS* and *MultiFoXS* (Schneidman-Duhovny *et al.*, 2013, 2016) were employed to calculate the scattering profile of hetero-parallel and hetero-antiparallel models. *Ab initio* bead density shape envelope models for each data set were initially generated within the *ATSAS* 3.2.1 package (Manalastas-Cantos *et al.*, 2021) by *DAMMIF* (Franke & Svergun, 2009), averaged over 23 independent runs using *DAMAVER* (Volkov & Svergun, 2003) and subsequently by a single *DAMMIN* (Svergun, 1999) run using expert mode with the radius of dummy atoms set to 5 Å. Envelopes were superimposed with structural models using *CIFSUP* (BioSAXS, EMBL) and the spatial resolution was estimated by *SASRES* (Tuukkanen *et al.*, 2016).

2.5. Protein crystallization

Crystallization screening was performed using a Crystal Gryphon robot (Art Robbins Instruments) with sitting-drop vapour-diffusion 96-well plates and commercial crystallization kits. Initial hits were further screened using low intervals of pH and concentration of PEG 3350 in sitting-drop, 24-well Intelli-Plates with a reservoir volume of 250 µl. Many different combinations and constructs of SEPT7 with its potential SEPT6-group partners were tested. Success was obtained for the case of SEPT14CC* with SEPT7CCext. The data presented here are from a crystal obtained in a 2 µl drop (1:1 protein:precipitant) employing a protein concentration of 16 mg ml^{-1} (1:1 molar ratio, 0.8 m*M* each, 7.3 mg ml^{-1} SEPT14CC*, 8.7 mg ml^{-1} SEPT7CCext) in 0.1 *M* bis-Tris pH 5.0, 24% PEG 3350. Plates were kept at 293 K and crystal growth was monitored by a Rock Imager 1000 (Formulatrix). Crystals were selected, transferred to the reservoir solution plus 20% PEG 200, cryocooled and stored in liquid nitrogen.

2.6. X-ray data collection, structure determination and refinement

X-ray data were collected by remote access through the ISPyB system on beamline I04 at DLS. Processing was carried out using *autoPROC* and *STARANISO* (Vonrhein *et al.*, 2018). Phasing was determined using polyalanine helices with *ARCIMBOLDO_LITE* (Caballero *et al.*, 2018) in coiled-coil mode, run through the *CCP4i* suite (Potterton *et al.*, 2003). Refinement was carried out with *BUSTER* (Global Phasing Ltd). Side-chain blobs from aromatic residues guided the determination of the register of the helices. Models were refined by iterative manual building into $2F_o - F_c$ and $F_o - F_c$ electron-density maps using *Coot* (Emsley *et al.*, 2010) and the refinement progress was followed with the use of R_{cryst} and R_{free} values. Torsion–libration–screw (TLS) motion restraints were applied throughout the final refinement steps. The final model quality was validated using *MolProbity* (Chen *et al.*, 2010).

2.7. Structural analysis and modelling

Crick angles (φ), coiled-coil periodicities and coiled-coil radii (half of the helix-to-helix distances) were extracted from the SEPT14CC*–SEPT7CCext crystal structure with *SamCC-Turbo* (Szczepaniak *et al.*, 2021). Crick angles from the hendecad portion in tetrabrachion (Stetefeld *et al.*, 2000; PDB entry 1fe6) were extracted with *SamCC-Turbo* and averaged by position. Values from heptads were taken from a compilation of parallel four-helix bundles (Szczepaniak *et al.*, 2018). These values (φ_0) were used for comparison. Core-packing angles were calculated by *Socket2* (Kumar & Woolfson, 2021) using a 8.0 Å cutoff. The radius of curvature of helices and supercoiling angles were measured with *HELANAL-Plus* (Kumar & Bansal, 2012) and *TWISTER* (Strelkov & Burkhard, 2002), respectively.

Table 1
Data collection and processing.

Values in parentheses are for the outer shell.

Diffraction source	I04, DLS
Wavelength (Å)	0.9795
Temperature (K)	100
Detector	EIGER2 XE 16M
Crystal-to-detector distance (mm)	294.97
Rotation range per image (°)	0.1
Total rotation range (°)	360
Exposure time per image (s)	0.008
Space group	$P2_1$
a, b, c (Å)	34.93, 50.81, 91.56
α, β, γ (°)	90.00, 94.36, 90.00
Mosaicity (°)	0.200
Anisotropy analysis	
Diffraction limits 1, 2, 3 (Å)	2.095, 1.949, 1.752
Direction 1†	0.7405, 0.0000, −0.6720; 0.363**a*** − 0.932**c***
Direction 2†	0.0000, 1.0000, 0.0000; **b***
Direction 3†	0.6720, 0.0000, 0.7405; 0.350**a*** + 0.937**c***
Resolution range (Å)	91.29–1.78 (1.97–1.78)
Total No. of reflections	152627 (6274)
No. of unique reflections	22355 (1118)
Completeness, spherical (%)	72.5 (14.2)
Completeness, ellipsoidal (%)	91.8 (52.8)
Multiplicity	6.8 (5.6)
$\langle I/\sigma(I)\rangle$	10.6 (1.3‡)
$CC_{1/2}$	0.999 (0.569)
$R_{r.i.m.}$	0.108 (1.289)
Overall B factor from Wilson plot (Å^2)	31.02

† Directions of principal axes of the ellipsoid expressed as direction cosines in the orthogonal basis following the PDB convention or in terms of reciprocal unit-cell vectors. ‡ $I/\sigma(I) \geq 2.0$ at 2.24 Å resolution.

Table 2
Structure solution and refinement.

PDB entry	8sjj
Resolution range (Å)	91.29–1.78
σ Cutoff	1.20
No. of reflections, working set	21214
No. of reflections, test set	1141 (5.1%)
Final R_{cryst} (%)	22.06
Final R_{free} (%)	28.63
Cruickshank DPI	0.204
No. of non-H atoms	
Protein	2654
Ion	8
Ligand	14
Water	247
Total	2923
R.m.s. deviations	
Bond lengths (Å)	0.008
Angles (°)	0.85
Average B factors (Å^2)	
Protein	39.2
Ion	49.9
Ligand	55.8
Water	37.8
Ramachandran plot	
Most favoured (%)	100
Allowed (%)	0

The coiled-coil models used for SEC–SAXS modelling and for structural comparison with the present structure were constructed with the deep-learning *AlphaFold-Multimer* methodology (Jumper *et al.*, 2021; Evans *et al.*, 2022) and were later relaxed with the Amber force field, with both steps using the Colab implementation (AlphaFold Google Colab) from Deepmind. Full-length septin pairs predicted to form coiled-coil-containing heterodimers were also modelled with *AlphaFold-Multimer* using *LocalColabFold* (Mirdita *et al.*, 2022). Hetero-antiparallel CCs were constructed with *CCBuilder* (Wood *et al.*, 2014). Domains were prepared and merged with *Coot* (Emsley *et al.*, 2010) and *PyMOL* (Schrödinger); the latter was used to prepare the structural figures.

3. Results and discussion

3.1. The SEPT14–SEPT7 coiled coil shows a strong preference for heterodimerization

Information regarding the different constructs used is presented in Fig. 1(*c*), Supplementary Fig. S2 and Supplementary Table S1. The CC peptides (SEPT14CC* and SEPT7CCext; 75 and 88 amino-acid residues, respectively) or an equimolar mixture of the two were found by SEC-MALS to be dimers in solution (Fig. 1*d*). To quantify their ability to heterodimerize, we conducted thermal denaturation CD spectroscopy experiments. Upon heterodimerization, there is usually a gain in the midpoint melting temperature (T_m) of the mixture compared with the average of the individual molecules (ΔT_m), as reported for the CTDs of SEPT6, SEPT8, SEPT10 and SEPT11 when combined in a 1:1 ratio with SEPT7C (de Almeida Marques *et al.*, 2012; Sala *et al.*, 2016). For SEPT14C, 1 m*M* DTT was added to the buffer to avoid oxidation of Cys345 and covalent homodimers. The measured T_m of the equimolar mixture of SEPT14C and SEPT7C was 48.5 ± 0.1°C, the highest of all CTD mixtures measured to date (Sala *et al.*, 2016), and 14.7 ± 0.3°C above the expected melting temperature if no heteromerization had occurred (Figs. 1*e* and 1*h*). When mixed, the crystallized constructs, SEPT14CC* and SEPT7CCext, also showed an increase in T_m of 15.4 ± 0.4°C (Figs. 1*f* and 1*h*). However, for a shorter SEPT7 construct (SEPT7CC*, 63 amino-acid residues) with SEPT14CC* heterodimerization was significantly impaired as judged by only a very limited increase in T_m (ΔT_m of 4.3 ± 0.5°C) in relation to the homodimers (Figs. 1*g* and 1*h*). This indicates that the residues at the N-terminus of the CC region are important in stabilizing the heterodimer.

3.2. Overall description of the coiled-coil structure

We crystallized and solved the structure of the heterodimeric CC formed between SEPT14 and SEPT7 (dubbed SEPT14CC*–SEPT7CCext here) at 1.78 Å resolution. Detailed data-collection and processing statistics are presented in Table 1. The data set was not twinned and was only mildly anisotropic. Phasing was preformed with *ARCIMBOLDO_LITE* (Caballero *et al.*, 2018) using polyalanine helices, resulting in good statistical indicators (LLG = 513, top TFZ = 11.2, final CC = 36.49%). Refinement statistics are summarized in Table 2. The asymmetric unit contains four chains (*A*–*D*), two of each peptide (SEPT14CC*, *A* and *B*; SEPT7CCext, *C* and *D*), giving rise to two crystallographically independent CC heterodimers (*AC* and *BD*). Both dimers are similar in

conformation and length, with an r.m.s.d. of 0.8 Å over 154 C^{α} atoms. The small differences are due to variation in the Crick angles in the two CCs, which are ∼14° towards the centre of the structures (Supplementary Fig. S3). The crystal packing is shown in Figs. 2(*a*) and 2(*b*).

Each heterodimeric CC comprises two long parallel helices of ∼110 and 120 Å for SEPT14CC* and SEPT7CCext, respectively (Figs. 2*c* and 2*d*). This parallel orientation was anticipated from the directions in which the unresolved CTDs emerge from the protofilament in the structure of the SEPT2G–SEPT6–SEPT7 complex (Mendonça *et al.*, 2021; Fig. 1*a*) as the SEPT14–SEPT7 dimer is equivalent to SEPT6–SEPT7. For the latter, this is consistent with FRET experiments between the CC domains (Low & Macara, 2006). In our new structure, however, essentially the entire sequences of both polypeptide chains are visible. SEPT7CCext, which is 13 residues longer than SEPT14CC*, has two extra α-helical turns at its N-terminus and a short nonhelical region at its C-terminus.

There are several interesting aspects of the structure, including the low supercoiling twist. More precisely, the structure has a slightly right-handed supercoil within its N-terminal half, which shifts to left-handed in the C-terminal half. As a result, the helices essentially lie side by side along the entire structure rather than having the supercoiling that is normally observed in traditional CCs. Consistent with the change in supercoiling, the two regions contain exclusively 11/3 (hendecad) and 7/2 (heptad) sequence repeats, respectively (Fig. 2*e*). Overall, the CC is slightly left-handed, with an overall supercoiling angle of ∼−50° (Fig. 2*f*). The SEPT14 helix is curved, with a radius of curvature of 185 Å.

3.2.1. Offset helices give rise to mixed layers. SEPT14 and SEPT7 have a sequence identity of 31% in the region revealed in our structure (Supplementary Fig. S2), despite being classified into two different septin groups. Interestingly, homologous positions do not pack against each other within the CC core (teal lines in Fig. 3*a*) due to an axial offset of one helical turn between the helices (SEPT7 is shifted towards its C-terminus). In addition, the packing geometry within core layers adds further asymmetry, as there are local helical rotations (Δφ, differences between the Crick angles for residues in the same layer) throughout the whole structure. This is enough to change the repeat position in one of the helices, giving rise to mixed layers. Despite these irregularities, S*ocket*2 (Kumar & Woolfson, 2021) and *SamCC-Turbo* (Szczepaniak *et al.*, 2021) automatically identify several CC interactions along the entire length of the structure (Supplementary Fig. S4 and Table S2).

The CC contains three complete hendecads followed by four complete heptads (Fig. 3*a*). The most N-terminal heptad in SEPT7 (the one closest to the hendecads) is more accurately assigned as *e*-*f*-*g*-*h*-*i*-*j*-*k*, instead of *a*-*b*-*c*-*d*-e-*f*-*g*. 18 core layers are present and, enumerating them from the N-terminus to the C-terminus, layers 1–11 and 12–18 are part of hendecads and heptads, respectively. Interestingly, the hendecads in the present structure are made of *a*-*d*-*h*-*k* cores (meaning that the *a*, *d*, *h* and *k* positions can participate in the core, although all four do not necessarily do so simultaneously

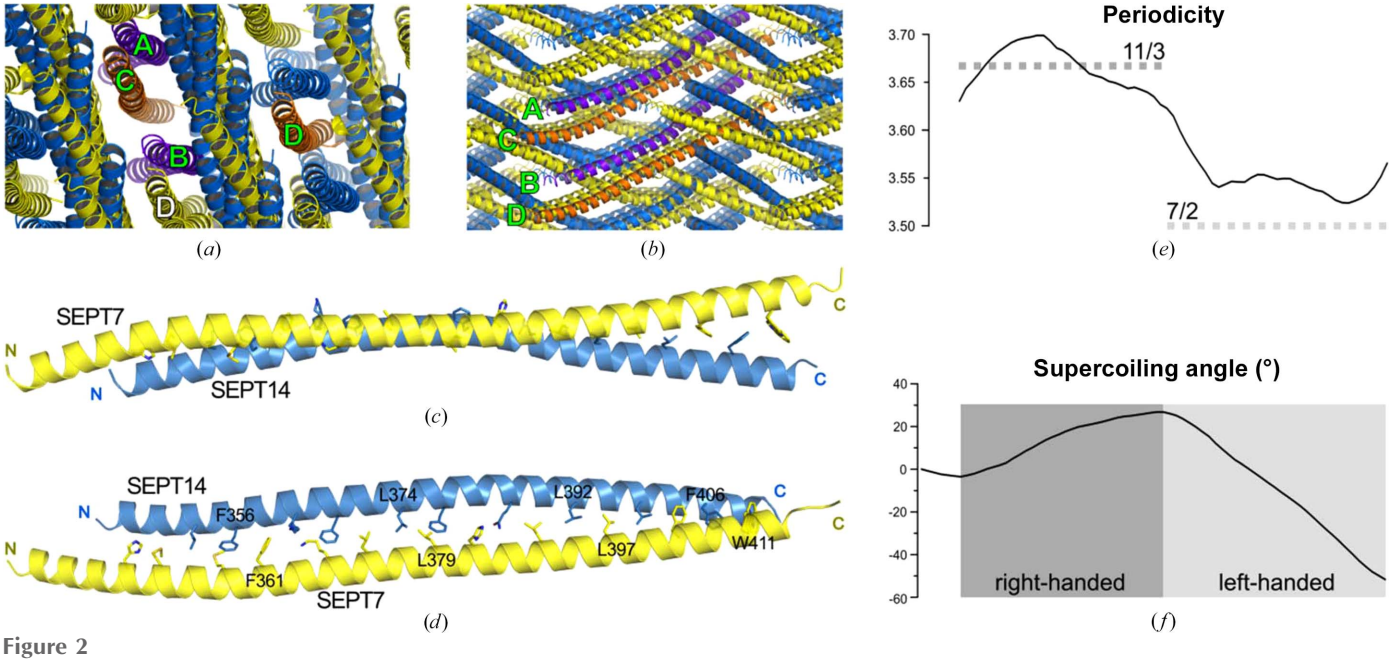

Figure 2
X-ray structure of the SEPT14CC*–SEPT7CCext heterodimeric CC. (*a*) Crystal packing viewed roughly along the CC axes and (*b*) perpendicular to the axes. Chains *A*, *B* (purple, SEPT14CC*), *C* and *D* (orange, SEPT7CCext) from the asymmetric unit are indicated (labelled in green). The *BD* dimer is formed using a *D* chain (labelled in white) which is shifted by a lattice translation with respect to the *D* chain of the asymmetric unit. The crystal packing is composed of alternate layers of CC heterodimers which are approximately aligned. (*c*) CC view orthogonal to the plane bisecting the helices and (*d*) rotated 90° in relation to (*c*). Blue, SEPT14CC*; yellow, SEPT7CCext. Only dimer *AC* and the side chains of positions *d* and *h* are shown. (*e*) Periodicities calculated by *SamCC-Turbo*, smoothed using a seven-residue window. (*f*) Cumulative supercoiling angle (in degrees); positive and negative first derivatives are related to right- and left-handed structures, respectively (indicated in grey boxes). The values displayed are an average between dimers *AC* and *BD*.

from any one repeat), which differs from the *a-d-e-h* cores seen in four-helix bundles (Stetefeld *et al.*, 2000; Lupas & Bassler, 2017), *i.e.* the *k* positions are incorporated into the core instead of the *e* positions (Supplementary Fig. S5). The Crick angles in the resulting core layers roughly agree with those found in hendecads of the tetrabrachion tetrameric structure (red dashed lines in Fig. 3*b*; Stetefeld *et al.*, 2000).

According to *Socket*2 (Kumar & Woolfson, 2021), the core-packing layers 1, 4 and 7 have parallel packing geometries, 2, 3, 6, 8, 9 and 11 have acute packing, and 5 and 10 have a *da-da*-like arrangement where two positions (in magenta; Fig. 3*b*) make KTK packing (Supplementary Fig. S6 and Table S2). The structure has a reduced number of KTK layers in the hendecad segment: one every five, instead of the expected one

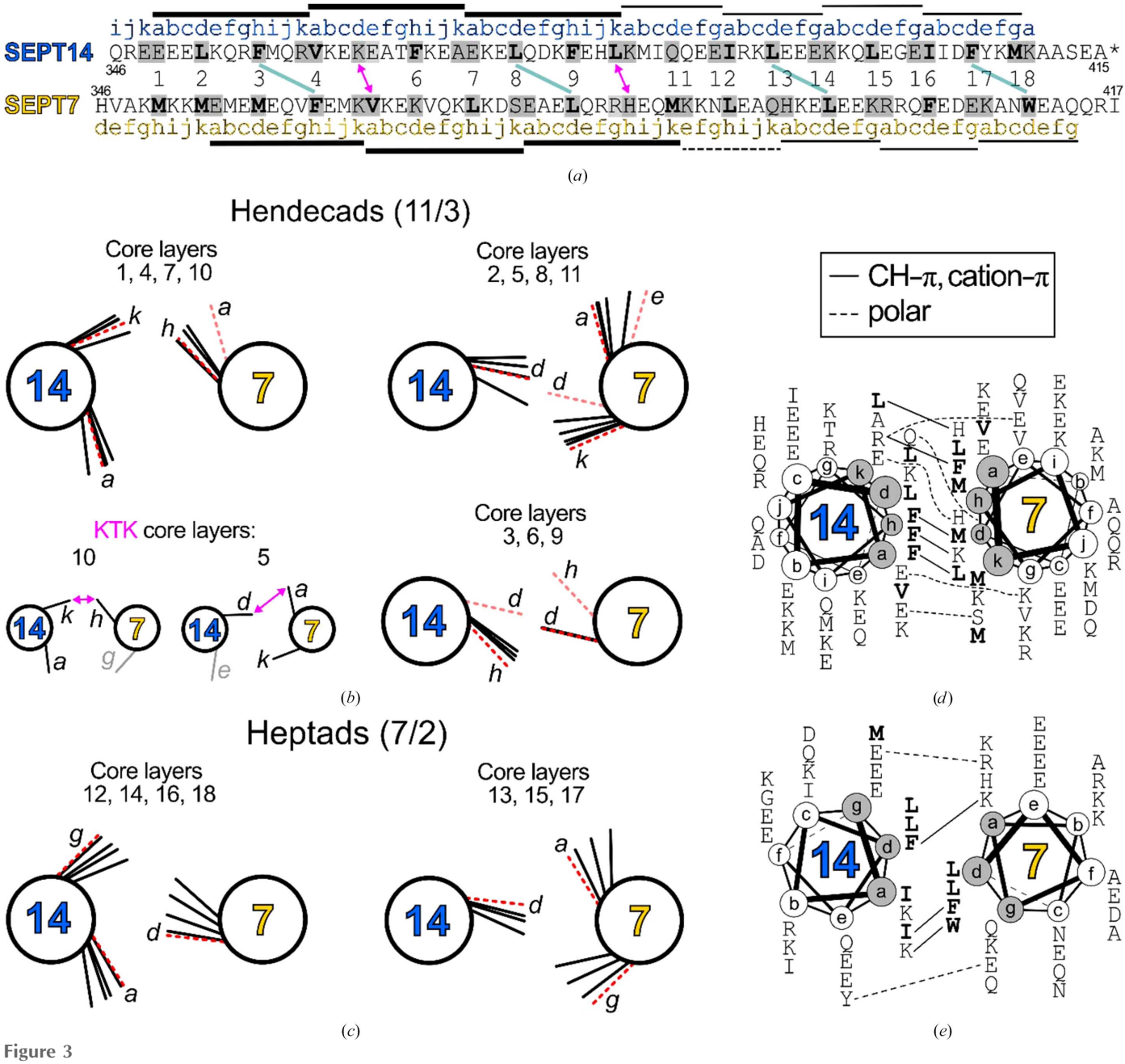

Figure 3
Register, core layers and interactions present in the SEPT14CC*–SEPT7CCext structure. (*a*) Register highlighting the core positions (grey) and genuine hydrophobic residues within the core (bold). Numbers in between sequences identify core layers. Thick and thin horizontal lines indicate hendecads and heptads, respectively. Both register and homologous positions (see the pairwise sequence alignment in Supplementary Fig. S2) have an axial shift of four residues in the same direction, indicated by the diagonal teal lines for selected reference positions. KTK interactions are indicated in core layers 5 and 10 (magenta arrows). (*b*) Scheme of core layers in the hendecads: core layers 1, 4, 7 and 10 (*h-ak* cores), 2, 5, 8 and 11 (*d-ak* cores) and 3, 6 and 9 (*d-h* cores). For core layers 5 and 10, the KTK interactions are highlighted (magenta) and a fourth site enters the core (light grey). (*c*) Scheme of core layers (12–18) in the heptads. The C^{α}–C^{β} vector is represented for each core position (black lines) as well as that found in comparative structures [φ_0, dashed red lines; from the tetrabrachion structure (PDB entry 1fe6) for (*b*) and from heptad-based four-helix bundles (Szczepaniak *et al.*, 2018) for (*c*)]. Helical wheel representation of the (*d*) hendecads and (*e*) heptads. Solid and dashed lines represent π and polar intermolecular interactions, respectively.

every three as seen in tetrabrachion. This is for two main reasons: the presence of long side chains allows their repositioning in relation to the C^{α}–C^{β} direction, and the off-centring of the knobs in other core layers. For example, core layers 3, 6 and 9 maintain KIH geometries but have *h* positions that are lopsided towards *d* positions. In the heptad region, the core layers have *d*-*ag* cores with rotated positions (*x* or *da* conformations) which pack with acute geometry. The Crick angles of these positions approach the expected values at the C-terminus (Fig. 3*c* and Supplementary Table S2).

3.2.2. The hydrophobic core is mainly composed of residues at the *d* and *h* positions. Another feature of the structure is that essentially only the *d* and *h* positions are occupied by hydrophobic residues. Mostly, there is just one hydrophobic residue in each core layer, and these are mainly leucines (nine) and phenylalanines (six). Residues in the other positions are mainly polar, including at the *a* sites. The presence of bulky side chains of phenylalanine at the *d* and *h* sites is related to the offset register, which guarantees that these do not become juxtaposed within a single layer. Layers 3, 6 and 9 have one aromatic residue (Phe) from SEPT14 paired against a non-aromatic residue (Met, Lys or Leu) from SEPT7 to make CH–π contacts, an interaction that is weaker (both in energy and directionality) than a hydrogen bond (Brandl *et al.*, 2001; Tsuzuki & Fujii, 2008). The other core layers with aromatic residues also have intermolecular CH–π or cation–π contacts (solid lines in Figs. 3*d* and 3*e*). These π interations have the expected geometry (average distance between carbon and the centre of the π system of 3.8 Å, σ = 0.3 Å).

There are a few hydrophilic residues in positions *d* or *h*, mainly in the hendecad portion. Lys363 at 14*d* (*i.e.* a *d* position in SEPT14) in layer 5 points out of the core and shows a *da*-*da*-like packing. Lys368 at 7*d* (layer 6) points out into solution. In the region where the repeats change from hendecads to heptads (layers 10 and 11), Gln385 at 14*d* points directly towards the SEPT7 helical axis (*x* conformation) and makes a hydrogen bond to the main-chain carbonyl of His383 at 7*h*. This histidine, another polar residue, is displaced away from the core, making a CH–π interaction with Leu381 (14*k*) in the KTK layer 10 (Supplementary Fig. S6). The residues in the *a* and *g*/*k* positions, *i.e.* *ak* pairs in the hendecads and *ag* pairs in heptads, are mostly hydrophilic and mainly charged (9 × Glu, 7 × Lys and 2 × Arg; a total of 18 out of 30). These residues, although described as part of the core, point towards the solvent, although some of them do participate in the formation of favourable intermolecular hydrogen bonds or electrostatic interactions (dashed lines; Figs. 3*d* and 3*e*).

3.3. SEC–SAXS experiments and *AlphaFold-multimer* modelling corroborate that the different heterodimeric septin coiled coils are parallel

An established principle in the septin field, known as Kinoshita's rule, dictates that other members of the SEPT6 group should be capable of substituting SEPT14 in forming heterodimers with SEPT7. However, despite many attempts, we have thus far been unsuccessful in obtaining diffraction-quality crystals of the remaining combinations (6–7, 8–7, 10–7 and 11–7). For this reason, we used small-angle X-ray scattering (SAXS) to glean structural insights, particularly with respect to the relative orientation of the helices.

SEC–SAXS experiments were carried out using a construct of the SEPT7 CTD fused to SUMO (dubbed SUMO-SEPT7c). This was used in equimolar mixtures together with each of the five different members of the SEPT6 group fused to MBP (SEPT6c, SEPT8c, SEPT10c, SEPT11c and SEPT14c; dubbed MBP-SEPT*X*c, *X* = 6, 8, 10, 11, 14; mixtures are referred to as *X*c-7c, for short). Both fusions were made at the N-terminus, connected to the CC region by a tripeptide linker. Therefore, in parallel structures both globular fusion proteins would appear at the same end of the CC, whereas antiparallel structures would be like a dumbbell. We reasoned that these would be readily distinguishable by SAXS. All relevant information regarding the SEC–SAXS data analysis is presented in Supplementary Table S3 and Fig. S7.

For all five samples, the SEC profile had a unique major peak eluting at similar volumes, with no evidence of aggregates. The radii of gyration (R_g) estimated from the Guinier plot and the $P(r)$ function ranged from 51.0 to 56.6 Å and from 56.0 to 60.4 Å, respectively, which are similar to the R_g values calculated from the *AlphaFold-Multimer* heterodimeric parallel model (53.5 Å). Calculated D_{max} values (199–217 Å) and the DATCLASS classification (extended) indicated that the heterodimers are elongated, as expected for CCs. Dimensionless Kratky plots indicate that the complexes are folded (Supplementary Fig. S7), and the masses calculated using the volume-of-correlation method (V_c; Rambo & Tainer, 2013) agree with the expected masses of the heterodimers (Supplementary Table S3).

Bead-density modelling gave 'lollipop' shapes, indicative of parallel CC assemblies considering the flexibility of the fusion proteins (Supplementary Fig. S8). Atomistic modelling with flexible linkers (Schneidman-Duhovny *et al.*, 2016) was consistent with heteroparallel dimers and generated acceptable statistics on fitting the experimental data (hetP, χ^2 = 1.29–1.61 with a higher value of χ^2 = 2.71 for 10c–7c). For the 10c–7c heterocomplex, the inclusion of a small proportion of homodimeric antiparallel MBP-SEPT10c (weight = 5.7%, R_g = 85.0 Å) slightly improves the fitting to the experimental data (χ^2 = 2.42) (Schneidman-Duhovny *et al.*, 2013). No such improvement was observed for the other four heterocomplexes, indicating essentially heterodimeric samples. A different behaviour for the 10c–7c heterodimer has been reported previously, in which the CD T_m gain of the mixture is not as evident (Fig. 1*h*) as for other CTD combinations (Sala *et al.*, 2016), suggesting that this particular combination may have slightly anomalous properties. We also considered the possibility of hetero-antiparallel dimers; however, these were unable to explain the data adequately (hetAP, χ^2 = 3.09–5.54; Fig. 4). All of these observations are in general agreement with the formation of parallel CCs for all five heterocomplexes.

Heterodimeric models for the five expected CTD septin heterocomplexes were constructed with *AlphaFold-Multimer*.

All five models generated for each heterocomplex were parallel and the best model possesses high confidence as measured by either the pLDDT (89–91) or the intermolecular PAE metrics (Supplementary Fig. S9). Modelling using full-length septin heterodimers also showed the formation of parallel heterodimeric CCs and septin subunits connected by an NC interface. This indicates that the *AlphaFold* models are not perturbed by the use of only the CTD and that the parallel arrangement described here for the heterodimeric coiled coils is consistent with the best available theoretical predictions. The models reproduce the register found in the present experimental structure for SEPT14CC*–SEPT7CCext, with homologous positions axially shifted by one helical turn. However, despite many similarities, the *AlphaFold-Multimer* and experimental models have small differences, including the lower curvature for SEPT14 in the former (a radius of curvature of 340 Å in the prediction against 185 Å in the experimental structure). Apparently related to this, the conformation of the side chain of Phe378 from SEPT14, at the centre of the curved helix, is particularly distinct: in the X-ray structure it points into the core (in both dimers) and in the predicted model it points to the solvent (Supplementary Fig. S9). Nevertheless, overall, the *AlphaFold*-predicted models reproduce the unusual properties of the dimer remarkably well.

3.4. Heterodimers are preferred over homodimers due to their longer coiled-coil length

Recently, the X-ray structure of the complete CTD of SEPT8 has been reported as a homodimer (Leonardo *et al.*, 2021). Only its central portion has interpretable electron density (74 out of 120 residues) and an even smaller region has CC contacts (60 residues). This is thought-provoking, given that an additional region of around 25 residues at the N-terminus is also consistent with the formation of CC assemblies (Sala *et al.*, 2016). As our new structure shows, a segment of this region included in SEPT14CC* does indeed make CC contacts, but apparently only when heterodimeric. Motivated by this, we compared SEPT14 in the present structure with SEPT8 in the homodimeric antiparallel structure (PDB entry 6wsm). This is justified on recalling that both SEPT14 and SEPT8 belong to the same septin group (SEPT6) and their CC regions have 55% sequence identity.

There is a match in the CC register for the most part, but due to the presence of only a single hendecad in the homodimeric structures (instead of at least three in the heterodimer), the positions become progressively out of register towards the N-terminus (Fig. 5*a*). For example, a conserved phenylalanine occupying an *h* position in the heterodimer (Phe356 in SEPT14) is out of the core in the homodimer (Phe348 in SEPT8), at a *g* position. The same happens with a leucine residue (Met344 in a *c* position in SEPT8), which occurs at *d* in the heterodimer (Fig. 5*b*). This is likely to be destabilizing and the SEPT8 antiparallel CC is not formed N-terminal to these residues (Leonardo *et al.*, 2021). A similar mechanism of 'frustrated' homodimers might also apply to SEPT7, although we cannot demonstrate this presently given the lack of a SEPT7 homodimeric CC structure.

The early interruption of the CC in homodimers might explain the preference for heterodimers that is seen in *vitro* (de Almeida Marques *et al.*, 2012; Sala *et al.*, 2016). In our heterodimeric structure, there is a consequent increase in the interface area and a decrease (more negative) in the Gibbs free energy (ΔG) of 25% and 35%, respectively, as estimated by *PISA* (Krissinel & Henrick, 2007), in comparison to the SEPT8 homodimeric CC. Based on this, the heterodimerization preference comes largely from the longer length of the heterodimer (~85 residues versus 60 residues; Fig. 5*c*; as also seen in SEPT6; PDB entry 6wbp). Additionally, by analysing the overall structure, there is an important rearrangement in the region where registers differ. This can also be understood by the distinct curvature of the helices between both structures: more curved in the heterodimer (SEPT14, radius of curvature of 185 Å) than in the homodimer (SEPT8, radius of curvature of 650 Å; Fig. 5*d*).

Additionally, we show the N-terminal region of the CC as necessary for SEPT14C–SEPT7C heterodimerization (Fig. 1*g*). Consistent with this, our attempts to solve the structure of the heterodimer using overtruncated peptides (such as

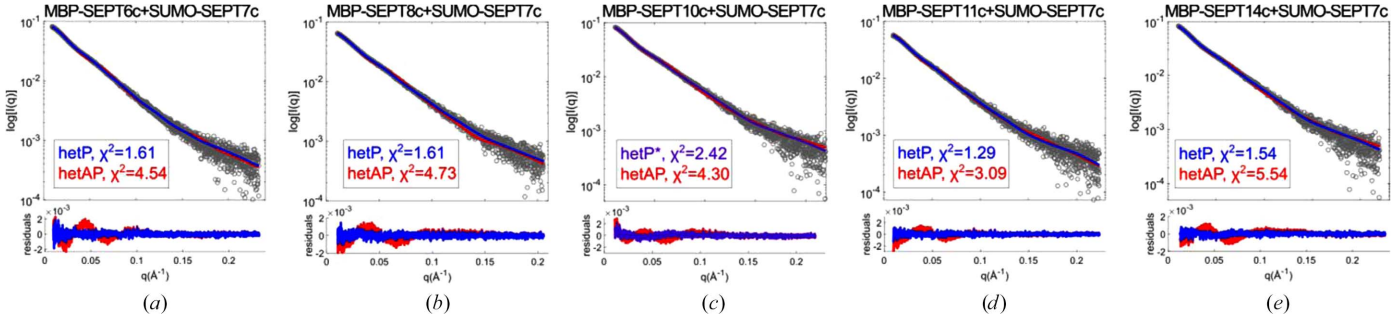

Figure 4
Atomistic modelling of the SEC–SAXS data. (*a*)–(*e*) Calculated scattering curves of hetero-parallel (hetP, blue) and hetero-antiparallel (hetAP, red) models were computed by *MultiFoXS* using flexible linkers. The residuals of the fitting to the experimental data (grey dots) are shown at the bottom. For the hetero-parallel solution of 10c–7c (*c*) (hetP*, purple), an ensemble of hetero-parallel (94.3%, model calculated previously with *MultiFoXS*) and MBP-fused homo-antiparallel dimers (5.7%, model based on the antiparallel homodimeric X-ray structure of SEPT8C, PDB entry 6wsm) was considered and calculated with *FoXS*. The χ^2 of the fit to the 10c–7c data improves slightly with the inclusion of homo-antiparallel dimers (from 2.71 to 2.42).

SEPT7CC*) were unsuccessful. This is an indication that constructs which lack this 25-residue region do not have a particularly strong tendency towards heterodimerization. The impact of this region might be twofold, providing additional stability to the heterodimer but also partially destabilizing homodimers due to the exposure of hydrophobic residues.

3.5. Implications for septin biology

Two regions with distinct periodicities are present in the structure: hendecads and heptads. Nonheptad periodicities might be key to the correct molecular recognition of CC-forming helices. This recognition is particularly important for septins, as they must select the correct NC partners (for example 6–7 and 2–2; Fig. 1*a*) from different nonphysiological ones (for example 2–6 and 2–7) and from heptad-based CCs present in other intracellular proteins. Nonphysiological arrangements, different to that shown in Fig. 1(*a*), may arise if this is not adequately controlled. Heterodimeric NC interfaces involving SEPT2-group members (2–6 and 2–7) are likely to be hampered not only by the length of the CCs but by the mismatch in periodicity towards the N-terminus, *i.e.* hendecads in SEPT6-group members and SEPT7 versus heptads in SEPT2-group members (Fig. 6). This is particularly noteworthy in the case of a potential 2–6 pairing because SEPT2-group members and SEPT7 have closely related G domains which also contribute to the NC interface (Mendonça *et al.*, 2021). A similar mechanism, where different CC periodicities seem to direct faithful protein–protein interactions, has been proposed for the correct pairing of cytoskeleton-associated proteins from *Giardia lamblia* (Hicks *et al.*, 1997). Thus, natural selection may have taken care of guaranteeing correct pairings by fine-tuning CCs in these ways.

Additionally, the presence of hendecad repeats seems to be relevant to the binding of partner proteins to septin oligomers and filaments. Hendecads broaden CC interfaces due to the slightly wider angular separation of the residues which make up the core positions (65° compared with 51°; Supplementary Fig. S10), potentially allowing other polypeptide chains to interact tightly with partially exposed dimeric cores. For this reason, these repeats are more favoured in higher-order oligomers. We have recently rationalized the binding interface of the BD3 motif of Borgs (binder of Rho GTPases) to the heterodimeric septin CC, aided by *AlphaFold* modelling of the ternary complex (Castro *et al.*, 2023). BD3 binds in the cavity between the CC helices, interacting exclusively with the hendecad segment and stabilizing the resulting ternary complex. The region of interaction is in the 14*a*/7*k* side (Fig. 3*d*) and it spans from core layers 3 to 10, as they are described here. The interaction with partners, such as Borgs, explains part of the irregularities of this CC structure: for example, in the predicted model of interaction a hydrophobic residue of the BD3 (Met/Leu, conserved in all five human Borgs) is inserted into one of the *da-da*-like core layers identified here (core layer 5). This type of interaction is only possible because of the wider binding surface provided by the hendecad region (Supplementary Fig. S10).

Our new structure appears to be a metastable state. This is apparent from the fact that it is devoid of tight core-layer interactions and lacks the supercoiling twist, in which the 'resilience to unfolding' present in long, twisted CCs is absent. The side-by-side helix–helix arrangement, which is also

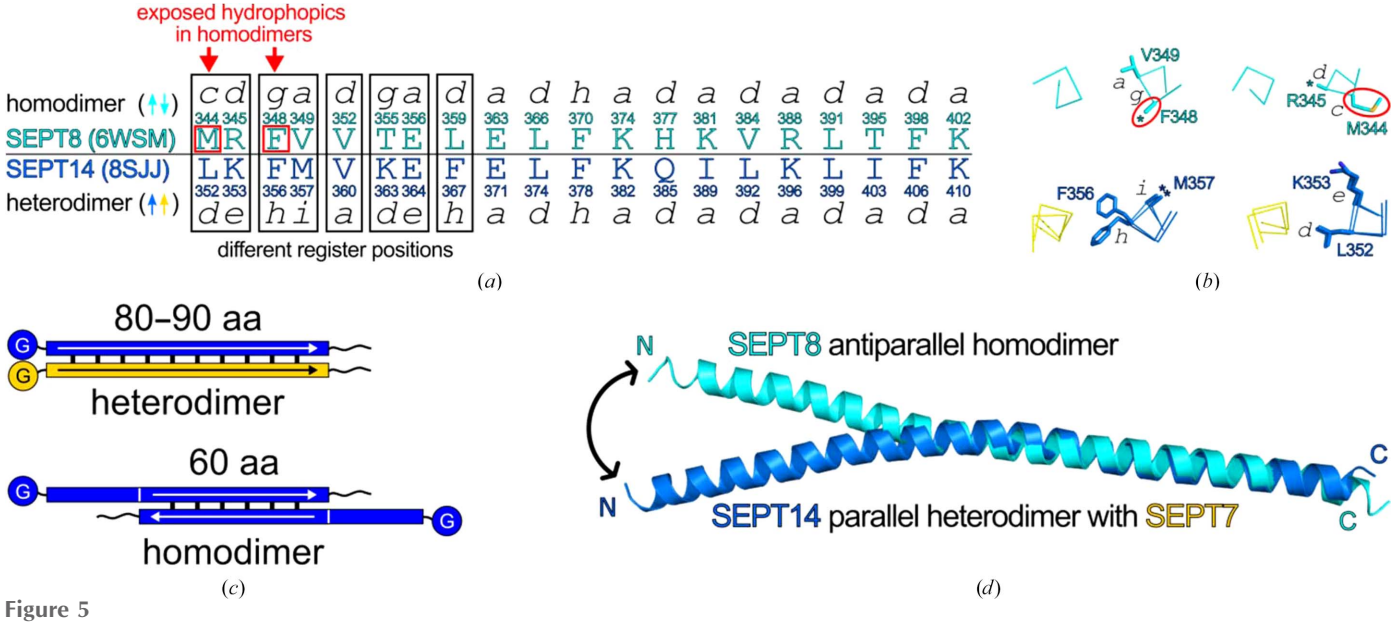

Figure 5
Register and length differences between homodimeric antiparallel (SEPT8; PDB entry 6wsm) and heterodimeric parallel (SEPT14–SEPT7; PDB entry 8sjj) septin CCs. (*a*) Comparison of core residues and positions. Core sites with different registers are highlighted in rectangles. Bulky hydrophobic residues (Met344 and Phe348 in SEPT8) are exposed in the homodimer (red). (*b*) Layers showing register differences in both structures. Nonmodelled residues due to the absence of electron density are indicated by asterisks (*). (*c*) Scheme representing the longer length of heterodimeric CCs in relation to homodimeric CCs. 'G' indicates the position of the G domain. (*d*) Structural comparison between the SEPT14 helix in the SEPT14–SEPT7 heterodimer and the SEPT8 helix in the SEPT8 homodimer. The region in which the homodimer and heterodimer have identical registers was used for structural alignment (towards the C-terminus). A reorientation of around 30° in the helical axis is necessary to go from one state to the other.

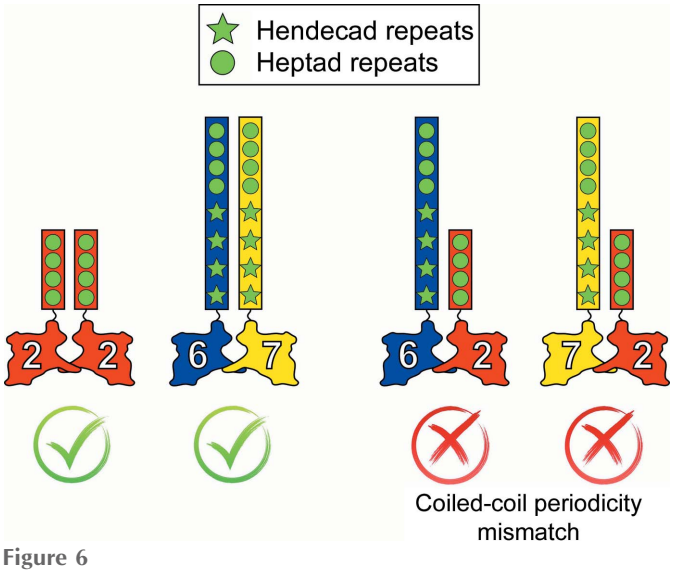

Figure 6
CC periodicities are important for septin recognition. SEPT2–SEPT2 and SEPT6–SEPT7 can assemble due to matching of periodicities (only heptads and hendecads/heptads at the N- and C-termini, respectively). Promiscuous, CC-containing NC interfaces, such as SEPT7–SEPT2 and SEPT6–SEPT2 (with the latter being particularly important, since SEPT2-group members are closely related to SEPT7), are disfavoured because of the different CC periodicities (hendecads versus heptads).

observed in both antiparallel homodimers of SEPT6 and SEPT8 and now in the parallel heterodimer, obviates the need for CC unwinding on transitioning between states acting as stabilizers of filaments during polymerization (parallel) and forming cross-bridges between them (antiparallel) during the assembly of higher-order structures (Leonardo *et al.*, 2021). Experimentally, parallel heterodimers seem to be preferred and here we have identified their greater length as at least part of the explanation for this. *In vivo*, however, this may also be a function of the presence of possible regulators of such states, including the presence of other septin filaments. Antiparallel homodimers, although shorter, might be more favourable when close to, for example, membranes due to partially burying polar residues in an environment of low dielectric constant, a hypothesis that we introduced recently (Leonardo *et al.*, 2021). On the other hand, the Borgs mentioned earlier are likely to stabilize and specify parallel heterodimers. The structural characterization of this CC fills an important gap in our current knowledge of septin biochemistry, confirming its parallel orientation and structurally justifying the specificity demonstrated by the septin NC heterodimeric interface.

4. Conclusion

Here, we have presented the first experimental structure of a heterodimeric septin coiled coil (CC). This comprises two C-terminal domains: a member of the SEPT6 group (SEPT6, SEPT8, SEPT10, SEPT11 and SEPT14) with SEPT7. The X-ray structure reveals a parallel heterodimeric CC between SEPT14 (SEPT14CC*) and SEPT7 (SEPT7CCext). As we describe, the unusual features of this noncanonical CC are highly suggestive of important roles related to septin function. These include how it controls correct filament assembly, the part it plays in orientational flipping to generate interfilament cross-bridges and its role in providing an appropriate binding surface for regulatory partner proteins such as Borgs. We also present SEC–SAXS data and *AlphaFold-Multimer* models supporting the parallel orientation for all five septin combinations expected to form heterodimeric CCs (6–7, 8–7, 10–7, 11–7 and 14–7), suggesting this to be a common feature and a corollary of Kinoshita's rule. In a filament, these would help stabilize the heterodimeric NC interface (Fig. 1*a*), although polymerization in their absence may happen under specific circumstances (Bertin *et al.*, 2010; Szuba *et al.*, 2021; Castro *et al.*, 2023). The structure described here, together with previous reports on septin CCs, sheds light on some of the potential control mechanisms associated with septin assembly and bundling. Further insight will require the determination of more high-resolution structures, and particularly single-particle cryo-EM studies and electron cryotomography of higher-order assemblies with the CC region ordered with respect to the filaments, thereby providing valuable information concerning their true role *in vivo*.

5. Data availability

The atomic coordinates and structure factors of the SEPT14–SEPT7 hetero CC structure have been deposited in the Protein Data Bank (PDB) under accession code 8sjj. The SAXS data have been deposited in the Small Angle Scattering Biological Data Bank (SASBDB) as entries SASDR39 (MBP-SEPT6c + SUMO-SEPT7c), SASDR49 (MBP-SEPT8c + SUMO-SEPT7c), SASDR59 (MBP-SEPT10c + SUMO-SEPT7c), SASDR69 (MBP-SEPT11c + SUMO-SEPT7c) and SASDR79 (MBP-SEPT14c + SUMO-SEPT7c). *AlphaFold-Multimer* models of the full-length septin heterodimers (6–7, 8–7, 10–7, 11–7 and 14–7) and the heterodimeric CTD coiled-coil complexes (6C–7C, 8C–7C, 10C–7C, 11C–7C and 14C–7C) are available in ModelArchive (https://modelarchive.org/) with the following accession codes: ma-ehtvp, ma-hv5qb, ma-i51oe, ma-rsp0h and ma-orsg7 (for the full-length septins) and ma-7fisk, ma-qnkm5, ma-q0d1q, ma-5x7mb and ma-zpgr8 (for the CTDs only), respectively.

Acknowledgements

The authors thank the participants of the CCP4 Macromolecular Crystallography School 2020 and the Alpbach Coiled Coil Workshop 2022 for exciting discussions and useful input. We kindly thank Instruct-ERIC (PID 18526) and iNEXT-Discovery (Sci-Tech) for enabling beamtime for crystal diffraction at I04 at the Diamond Light Source (DLS) synchrotron. The I04 and B21 beamline specialists and DLS staff are also greatly acknowledged. This study made use of NMRbox (NIH).

Funding information

FAPESP ('Fundação de Amparo à Pesquisa do Estado de São Paulo') is acknowledged for financial support through grants

2018/19992-7 and 2022/00262-4 (IAC), 2014/15546-1 and 2020/02897-1 (RCG). We also thank the BBSRC (Biotechnology and Biological Sciences Research Council), BB/W008823/1 (AJW).

References

Almeida Marques, I., Valadares, N. F., Garcia, W., Damalio, J. C. P., Macedo, J. N. A., Araújo, A. P. U., Botello, C. A., Andreu, J. M. & Garratt, R. C. (2012). *Cell Biochem. Biophys.* **62**, 317–328.

Beesley, J. L. & Woolfson, D. N. (2019). *Curr. Opin. Biotechnol.* **58**, 175–182.

Bertin, A., McMurray, M. A., Grob, P., Park, S. S., Garcia, G., Patanwala, I., Ng, H. L., Alber, T., Thorner, J. & Nogales, E. (2008). *Proc. Natl Acad. Sci. USA*, **105**, 8274–8279.

Bertin, A., McMurray, M. A., Thai, L., Garcia, G., Votin, V., Grob, P., Allyn, T., Thorner, J. & Nogales, E. (2010). *J. Mol. Biol.* **404**, 711–731.

Brandl, M., Weiss, M. S., Jabs, A., Sühnel, J. & Hilgenfeld, R. (2001). *J. Mol. Biol.* **307**, 357–377.

Brown, J. H., Cohen, C. & Parry, D. A. D. (1996). *Proteins*, **26**, 134–145.

Caballero, I., Sammito, M., Millán, C., Lebedev, A., Soler, N. & Usón, I. (2018). *Acta Cryst.* D**74**, 194–204.

Castro, D. K. S. V., Rosa, H. V. D., Mendonça, D. C., Cavini, I. A., Araujo, A. P. U. & Garratt, R. C. (2023). *J. Mol. Biol.* **435**, 168132.

Cavini, I. A., Leonardo, D. A., Rosa, H. V. D., Castro, D. K. S. V., D'Muniz Pereira, H., Valadares, N. F., Araujo, A. P. U. & Garratt, R. C. (2021). *Front. Cell. Dev. Biol.* **9**, 765085.

Chen, V. B., Arendall, W. B., Headd, J. J., Keedy, D. A., Immormino, R. M., Kapral, G. J., Murray, L. W., Richardson, J. S. & Richardson, D. C. (2010). *Acta Cryst.* D**66**, 12–21.

Cowieson, N. P., Edwards-Gayle, C. J. C., Inoue, K., Khunti, N. S., Doutch, J., Williams, E., Daniels, S., Preece, G., Krumpa, N. A., Sutter, J. P., Tully, M. D., Terrill, N. J. & Rambo, R. P. (2020). *J. Synchrotron Rad.* **27**, 1438–1446.

Crick, F. H. C. (1952). *Nature*, **170**, 882–883.

Crick, F. H. C. (1953). *Acta Cryst.* **6**, 689–697.

Emsley, P., Lohkamp, B., Scott, W. G. & Cowtan, K. (2010). *Acta Cryst.* D**66**, 486–501.

Evans, R., O'Neill, M., Pritzel, A., Antropova, N., Senior, A., Green, T., Žídek, A., Bates, R., Blackwell, S., Yim, J., Ronneberger, O., Bodenstein, S., Zielinski, M., Bridgland, A., Potapenko, A., Cowie, A., Tunyasuvunakool, K., Jain, R., Clancy, E., Kohli, P., Jumper, J. & Hassabis, D. (2022). *bioRxiv*, 2021.10.04.463034.

Fischer, H., de Oliveira Neto, M., Napolitano, H. B., Polikarpov, I. & Craievich, A. F. (2010). *J. Appl. Cryst.* **43**, 101–109.

Franke, D. & Svergun, D. I. (2009). *J. Appl. Cryst.* **42**, 342–346.

Hajizadeh, N. R., Franke, D., Jeffries, C. M. & Svergun, D. I. (2018). *Sci. Rep.* **8**, 7204.

Harbury, P. B., Zhang, T., Kim, P. S. & Alber, T. (1993). *Science*, **262**, 1401–1407.

Harrison, C. J., Hayer-Hartl, M., Liberto, M. D., Hartl, F. U. & Kuriyan, J. (1997). *Science*, **276**, 431–435.

Hartwell, L. H. (1971). *Exp. Cell Res.* **69**, 265–276.

Hicks, M. R., Holberton, D. V., Kowalczyk, C. & Woolfson, D. N. (1997). *Fold. Des.* **2**, 149–158.

Hopkins, J. B., Gillilan, R. E. & Skou, S. (2017). *J. Appl. Cryst.* **50**, 1545–1553.

Hu, Q., Milenkovic, L., Jin, H., Scott, M. P., Nachury, M. V., Spiliotis, E. T. & Nelson, W. J. (2010). *Science*, **329**, 436–439.

Jiao, F., Cannon, K. S., Lin, Y., Gladfelter, A. S. & Scheuring, S. (2020). *Nat. Commun.* **11**, 5062.

Jumper, J., Evans, R., Pritzel, A., Green, T., Figurnov, M., Ronneberger, O., Tunyasuvunakool, K., Bates, R., Žídek, A., Potapenko, A., Bridgland, A., Meyer, C., Kohl, S. A. A., Ballard, A. J., Cowie, A., Romera-Paredes, B., Nikolov, S., Jain, R., Adler, J., Back, T., Petersen, S., Reiman, D., Clancy, E., Zielinski, M., Steinegger, M., Pacholska, M., Berghammer, T., Bodenstein, S., Silver, D., Vinyals, O., Senior, A. W., Kavukcuoglu, K., Kohli, P. & Hassabis, D. (2021). *Nature*, **596**, 583–589.

Kim, M. S., Froese, C. D., Estey, M. P. & Trimble, W. S. (2011). *J. Cell Biol.* **195**, 815–826.

Kinoshita, M. (2003). *J. Biochem.* **134**, 491–496.

Krissinel, E. & Henrick, K. (2007). *J. Mol. Biol.* **372**, 774–797.

Kumar, P. & Bansal, M. (2012). *J. Biomol. Struct. Dyn.* **30**, 773–783.

Kumar, P. & Woolfson, D. N. (2021). *Bioinformatics*, **37**, 4575–4577.

Leonardo, D. A., Cavini, I. A., Sala, F. A., Mendonça, D. C., Rosa, H. V. D., Kumagai, P. S., Crusca, E., Valadares, N. F., Marques, I. A., Brandão-Neto, J., Munte, C. E., Kalbitzer, H. R., Soler, N., Usón, I., André, I., Araujo, A. P. U., D'Muniz Pereira, H. & Garratt, R. C. (2021). *J. Mol. Biol.* **433**, 166889.

Lin, Y.-H., Huang, C.-Y., Ke, C.-C., Wang, Y.-Y., Lai, T.-H., Liu, H.-C., Ku, W.-C., Chan, C.-C. & Lin, Y.-H. (2020). *Biomedicines*, **8**, 518.

Liu, J., Deng, Y., Zheng, Q., Cheng, C. S., Kallenbach, N. R. & Lu, M. (2006). *Biochemistry*, **45**, 15224–15231.

Low, C. & Macara, I. G. (2006). *J. Biol. Chem.* **281**, 30697–30706.

Lupas, A. (1996). *Trends Biochem. Sci.* **21**, 375–382.

Lupas, A. N. & Bassler, J. (2017). *Trends Biochem. Sci.* **42**, 130–140.

Lupas, A. N. & Gruber, M. (2005). *Adv. Protein Chem.* **70**, 37–78.

Manalastas-Cantos, K., Konarev, P. V., Hajizadeh, N. R., Kikhney, A. G., Petoukhov, M. V., Molodenskiy, D. S., Panjkovich, A., Mertens, H. D. T., Gruzinov, A., Borges, C., Jeffries, C. M., Svergun, D. I. & Franke, D. (2021). *J. Appl. Cryst.* **54**, 343–355.

Martinez, C. & Ware, J. (2004). *Exp. Biol. Med. (Maywood)*, **229**, 1111–1119.

Mendonça, D. C., Guimarães, S. L., Pereira, H. D. M., Pinto, A. A., de Farias, M. A., de Godoy, A. S., Araujo, A. P. U., van Heel, M., Portugal, R. V. & Garratt, R. C. (2021). *J. Mol. Biol.* **433**, 167096.

Mendonça, D. C., Macedo, J. N., Guimarães, S. L., Barroso da Silva, F. L., Cassago, A., Garratt, R. C., Portugal, R. V. & Araujo, A. P. U. (2019). *Cytoskeleton*, **76**, 457–466.

Mirdita, M., Schütze, K., Moriwaki, Y., Heo, L., Ovchinnikov, S. & Steinegger, M. (2022). *Nat. Methods*, **19**, 679–682.

Mostowy, S. & Cossart, P. (2012). *Nat. Rev. Mol. Cell Biol.* **13**, 183–194.

Noell, C. R., Loh, J. Y., Debler, E. W., Loftus, K. M., Cui, H., Russ, B. B., Zhang, K., Goyal, P. & Solmaz, S. R. (2019). *J. Phys. Chem. Lett.* **10**, 4362–4367.

Ong, K., Wloka, C., Okada, S., Svitkina, T. & Bi, E. (2014). *Nat. Commun.* **5**, 5698.

Pan, F., Malmberg, R. L. & Momany, M. (2007). *BMC Evol. Biol.* **7**, 103.

Pauling, L. & Corey, R. B. (1953). *Nature*, **171**, 59–61.

Peters, J., Baumeister, W. & Lupas, A. (1996). *J. Mol. Biol.* **257**, 1031–1041.

Peterson, E. A., Kalikin, L. M., Steels, J. D., Estey, M. P., Trimble, W. S. & Petty, E. M. (2007). *Mamm. Genome*, **18**, 796–807.

Potterton, E., Briggs, P., Turkenburg, M. & Dodson, E. (2003). *Acta Cryst.* D**59**, 1131–1137.

Rambo, R. P. & Tainer, J. A. (2013). *Nature*, **496**, 477–481.

Robertin, S. & Mostowy, S. (2020). *Cell. Microbiol.* **22**, e13173.

Sala, F. A., Valadares, N. F., Macedo, J. N. A., Borges, J. C. & Garratt, R. C. (2016). *Biophys. J.* **111**, 2608–2619.

Schneidman-Duhovny, D., Hammel, M., Tainer, J. A. & Sali, A. (2013). *Biophys. J.* **105**, 962–974.

Schneidman-Duhovny, D., Hammel, M., Tainer, J. A. & Sali, A. (2016). *Nucleic Acids Res.* **44**, W424–W429.

Sellin, M. E., Sandblad, L., Stenmark, S. & Gullberg, M. (2011). *Mol. Biol. Cell*, **22**, 3152–3164.

Shafipour, M., Sabbaghian, M., Shahhoseini, M. & Sadighi Gilani, M. A. (2014). *Iran. J. Reprod. Med.* **12**, 205–208.

Sirajuddin, M., Farkasovsky, M., Hauer, F., Kühlmann, D., Macara, I. G., Weyand, M., Stark, H. & Wittinghofer, A. (2007). *Nature*, **449**, 311–315.

Soroor, F., Kim, M. S., Palander, O., Balachandran, Y., Collins, R. F., Benlekbir, S., Rubinstein, J. L. & Trimble, W. S. (2021). *Mol. Biol. Cell*, **32**, 289–300.
Stetefeld, J., Jenny, M., Schulthess, T., Landwehr, R., Engel, J. & Kammerer, R. A. (2000). *Nat. Struct. Biol.* **7**, 772–776.
Strelkov, S. V. & Burkhard, P. (2002). *J. Struct. Biol.* **137**, 54–64.
Svergun, D. I. (1999). *Biophys. J.* **76**, 2879–2886.
Szczepaniak, K., Bukala, A., da Silva Neto, A. M., Ludwiczak, J. & Dunin-Horkawicz, S. (2021). *Bioinformatics*, **36**, 5368–5376.
Szczepaniak, K., Ludwiczak, J., Winski, A. & Dunin-Horkawicz, S. (2018). *J. Struct. Biol.* **204**, 117–124.
Szuba, A., Bano, F., Castro-Linares, G., Iv, F., Mavrakis, M., Richter, R. P., Bertin, A. & Koenderink, G. H. (2021). *eLife*, **10**, e63349.
Tsuzuki, S. & Fujii, A. (2008). *Phys. Chem. Chem. Phys.* **10**, 2584–2594.
Tully, M. D., Tarbouriech, N., Rambo, R. P. & Hutin, S. (2021). *J. Vis. Exp.*, e61578.
Tuukkanen, A. T., Kleywegt, G. J. & Svergun, D. I. (2016). *IUCrJ*, **3**, 440–447.
Uhlén, M., Fagerberg, L., Hallström, B. M., Lindskog, C., Oksvold, P., Mardinoglu, A., Sivertsson, Å., Kampf, C., Sjöstedt, E., Asplund, A., Olsson, I. M., Edlund, K., Lundberg, E., Navani, S., Szigyarto, C. A. K., Odeberg, J., Djureinovic, D., Takanen, J. O., Hober, S., Alm, T., Edqvist, P. H., Berling, H., Tegel, H., Mulder, J., Rockberg, J., Nilsson, P., Schwenk, J. M., Hamsten, M., von Feilitzen, K., Forsberg, M., Persson, L., Johansson, F., Zwahlen, M., von Heijne, G., Nielsen, J. & Pontén, F. (2015). *Science*, **347**, 1260419.
Vahabi Barzi, N., Kakavand, K., Sodeifi, N., Ghezelayagh, Z. & Sabbaghian, M. (2020). *Reprod. Biol.* **20**, 164–168.
Valadares, N. F., d'Muniz Pereira, H., Ulian Araujo, A. P. & Garratt, R. C. (2017). *Biophys. Rev.* **9**, 481–500.
Versele, M., Gullbrand, B., Shulewitz, M. J., Cid, V. J., Bahmanyar, S., Chen, R. E., Barth, P., Alber, T. & Thorner, J. (2004). *Mol. Biol. Cell*, **15**, 4568–4583.
Volkov, V. V. & Svergun, D. I. (2003). *J. Appl. Cryst.* **36**, 860–864.
Vonrhein, C., Tickle, I. J., Flensburg, C., Keller, P., Paciorek, W., Sharff, A. & Bricogne, G. (2018). *Acta Cryst.* A**74**, a360.
Wang, Y.-Y., Lai, T.-H., Chen, M.-F., Lee, H.-L., Kuo, P.-L. & Lin, Y.-H. (2019). *J. Clin. Med.* **8**, 1297.
Wood, C. W., Bruning, M., Ibarra, A. A., Bartlett, G. J., Thomson, A. R., Sessions, R. B., Brady, R. L. & Woolfson, D. N. (2014). *Bioinformatics*, **30**, 3029–3035.
Woolfson, D. N. (2017). *Subcell. Biochem.* **82**, 35–61.
Woolfson, D. N. (2023). *J. Biol. Chem.* **299**, 104579.